nanomaterials

MDPI

Article

Electrostatic and Environmental Control of the Trion Fine Structure in Transition Metal Dichalcogenide Monolayers

Yaroslav V. Zhumagulov [1,*], Alexei Vagov [2], Dmitry R. Gulevich [3] and Vasili Perebeinos [4,*]

[1] Faculty of Physics, University of Regensburg, 93040 Regensburg, Germany
[2] Faculty of Physics, National Research University Higher School of Economics, 101000 Moscow, Russia
[3] ITMO University, 197101 St. Petersburg, Russia
[4] Department of Electrical Engineering, University at Buffalo, The State University of New York, Buffalo, NY 14260, USA
* Correspondence: iaroslav.zhumagulov@physik.uni-regensburg.de (Y.V.Z.); vasilipe@buffalo.edu (V.P.)

Abstract: Charged excitons or trions are essential for optical spectra in low-dimensional doped monolayers (ML) of transitional metal dichalcogenides (TMDC). Using a direct diagonalization of the three-body Hamiltonian, we calculate the low-lying trion states in four types of TMDC MLs as a function of doping and dielectric environment. We show that the fine structure of the trion is the result of the interplay between the spin-valley fine structure of the single-particle bands and the exchange interaction. We demonstrate that by variations of the doping and dielectric environment, the fine structure of the trion energy can be tuned, leading to anticrossing of the bright and dark states, with substantial implications for the optical spectra of the TMDC ML.

Keywords: excitons; trions; transition metal dichalcogenides

Citation: Zhumagulov, Y.V.; Vagov, A.; Gulevich, D.R.; Perebeinos, V. Electrostatic and Environmental Control of the Trion Fine Structure in Transition Metal Dichalcogenide Monolayers. *Nanomaterials* **2022**, *12*, 3728. https://doi.org/10.3390/nano12213728

Academic Editor: Giancarlo Soavi

Received: 28 September 2022
Accepted: 19 October 2022
Published: 24 October 2022

1. Introduction

The 2D geometry of TMDC ML significantly enhances the Coulomb interaction, leading to a much higher exciton binding energy [1–6] compared to bulk semiconductors [7–9]. 2D confinement also facilitates other many-body states, including three-particle trions [10–19] and four-particle biexcitons [20–26] with high binding energies. Experiments and theoretical calculations demonstrated that the lowest-energy optical excitations in a doped TMDC ML are often associated with trions [10–19]. A sophisticated band structure with two direct band gaps at the K and $K' = -K$ points of the Brillouin zone and the presence of the spin valley locking effect [27–30] allow various trionic states to be realized in the TMDC ML [31–45]. Commonly, trions are classified by spin and valley quantum numbers, and they can be dark or bright depending on the combination of the quantum numbers. The trionic fine structure determines the optical absorption edge and the photoluminescence spectra. In particular, the photoluminescence spectra strongly depend on whether the ground trion state is optically bright or dark.

The low energy trion spectra in TMDC MLs are crucially dependent on multiple factors, such as spin-orbit coupling, direct and exchange Coulomb interactions, and carrier doping level. The dark- and bright-state energies determine the spectral properties of TMDC, particularly the temperature behavior of the photoluminescence spectra [40,46–48]. The internal structure of the trion states makes them optically dark or bright, depending on the valley and spin configuration. Because of the small energy differences, these states are difficult to distinguish experimentally, especially at elevated temperatures and in samples with a significant number of defects. For the same reasons, it is not easy to accurately calculate the trion states' relative positions. For example, MoS2 ML theories [36,39,49] predict different types of the lowest energy trion states. The experiments observe bright trions in the photoluminesce spectra, and positions of the dark states can only be inferred from an additional set of measurements, such as temperature dependence of the photoluminescence intensity [32] or excited state dynamics [50].

This work presents a comprehensive theoretical analysis of the three-particle states in TMDC MLs. We find that the low-energy fine structure of trions depends not only on the material-specific band structure but also on the doping and dielectric environment. The calculated trion states are mainly controlled by the interaction of spin-orbit splitting and exchange interactions, which depend on doping and the environment. The most nontrivial situation arises when the spin-orbit splitting is small and negative, as in MoS2 ML. In this case, we find that the low-lying trion states are close to degeneracy, allowing the possibility of switching the relative positions of the dark and bright states by varying the external gate voltage in a field-effect transistor setup on different dielectric substrates. However, because the predicted tunability range of energies is only a few meV, the design of low-temperature experiments using homogeneous samples with low defect density is needed to observe the anticrossing phenomena. While bright trions reveal themselves in the photoluminesce spectra, additional measurements are needed, such as temperature dependence of the photoluminesce, excited states dynamics, or non-linear spectroscopy to probe the dark states. Thin oxide dielectrics can help to establish higher gate capacitance for a broader range of Fermi-level tunability.

2. Materials and Methods: Three-Particle States in TMDC Monolayers

The calculation of trion states is performed by a direct diagonalization of the three-body Hamiltonian obtained by spanning the many-body model into states with two electrons and a hole (we consider negatively charged trions) $|c_1c_2v\rangle = a^\dagger_{c_1}a^\dagger_{c_2}a_v|0\rangle$, where $c_{1,2}$ and v are single-particle electron and hole states. The ground state $|0\rangle$ has a filled valence band and an empty conduction band. The Hamiltonian reads as follows.

$$\begin{aligned} H &= H_0 + H_{cc} + H_{cv}, \\ H_0 &= +(\varepsilon_{c_1} + \varepsilon_{c_2} - \varepsilon_v)\delta^{c_1'}_{c_1}\delta^{c_2'}_{c_2}\delta^{v'}_{v}, \\ H_{cc} &= +(W^{c_1'c_2'}_{c_1c_2} - W^{c_2'c_1'}_{c_1c_2})\delta^{v'}_{v}, \\ H_{cv} &= -(W^{vc_1'}_{v'c_1} - V^{c_1'v}_{v'c_1})\delta^{c_2'}_{c_2} - (W^{vc_2'}_{v'c_2} - V^{c_2'v}_{v'c_2})\delta^{c_1'}_{c_1} \\ &\quad + (W^{vc_2'}_{v'c_1} - V^{c_2'v}_{v'c_1})\delta^{c_1'}_{c_2} + (W^{vc_1'}_{v'c_2} - V^{c_1'v}_{v'c_2})\delta^{c_2'}_{c_1}, \end{aligned} \tag{1}$$

where $\varepsilon_{c,v}$ are single-particle energies, W and V are the screened and bare Coulomb potentials. The latter is given by $V^{ab}_{cd} = V(\mathbf{k}_a - \mathbf{k}_c)\langle u_c|u_a\rangle\langle u_d|u_b\rangle$ with $\langle u_c|u_a\rangle$ and the overlap of the Bloch states of a single particle and $V(q) = 2\pi e^2/q$. For the intravalley screened potential, we follow Reference [51] and substitute $V(q)$ in this expression by the Rytova-Keldysh $W(q)$ potential [52–55]

$$W(q) = V(q)\begin{cases} \varepsilon^{-1}_{env}(1 + r_0 q)^{-1} & q - \text{intravalley} \\ \varepsilon^{-1}_{bulk} & q - \text{interavalley} \end{cases}, \tag{2}$$

where "intravalley" stands for the states within the same valley and "intervalley" stands for states in different valleys. For the encapsulating material, the effective dielectric constant $\varepsilon_{env} = (\varepsilon_2 + \varepsilon_1)/2$ is the average of dielectric constants on both sides of the ML, and the screening length is $r_0 = \varepsilon_{bulk}d/(2\varepsilon_{env})$ with d being the width of the ML [51,56]. Notice that the finite-intervalley dielectric screening induces the intervalley interaction between pairs of trion states. It was not observed in previous works where only the Keldysh potential was used [40,57].

For the single-particle states, we assume the massive $k \cdot p$ Dirac model [58]

$$\begin{aligned} H_0 &= v_F\hat{s}_0 \otimes \left(\tau k_x\hat{\sigma}_x + k_y\hat{\sigma}_y\right) + \frac{\Delta}{2}\hat{s}_0 \otimes \hat{\sigma}_z \\ &\quad + \frac{1}{2}\tau\hat{s}_z \otimes [\lambda_c(\hat{\sigma}_0 + \hat{\sigma}_z) + \lambda_v(\hat{\sigma}_0 - \hat{\sigma}_z)], \end{aligned} \tag{3}$$

where $\hat{\sigma}_i$ are the Pauli matrices in the band subspace, $\hat{s}_z$ is the Pauli matrix in the spin subspace, $\hat{\sigma}_0$ and $\hat{s}_0$ are unity matrices, $\tau = \pm 1$ is the valley index for K and $K' = -K$, v_F is the effective Fermi velocity, and Δ is the bandgap. The last contribution to Equation (3) describes the Zeeman spin-orbit coupling with constants $\lambda_{c,v}$. The parameters Δ and $\lambda_{c,v}$ are obtained by fitting the ab initio band structure calculations using the DFT / GW approaches [59–61]. The gap Δ depends on the encapsulating materials and needs a correction, for example, using the scissor operator approach, when quantitatively accurate results are required [56]. It is known that the dielectric environment does not change the effective mass of the single-particle states [62]. To reflect this fact, the effective Fermi velocity is chosen as $v_F = \sqrt{\Delta/2m}$. Pauli blocking accounts for doping in a finite-grid mesh of the reciprocal space [40,57,63]. The dipole matrix elements needed to calculate the oscillator strength are obtained from the trion wavefunctions. Further details of the calculations can be found in Appendices A and B, and the model parameters, extracted from the first-principles calculations for TMDC ML, are summarized in Table 1.

Table 1. Model parameters for TMDC MLs: lattice constant a, effective mass m in units of free electron mass m_e, and spin-orbit couplings $\lambda_{c,v}$ are taken from Reference [61]. The layer thickness d and bulk dielectric constant ε_{bulk} are from Reference [64], and bandgap Δ_0 is from Reference [60] (see model (3)).

	a [Å]	d [Å]	ε_{bulk}	Δ_0 [eV]	m/m_e	λ_c [meV]	λ_v [meV]
MoS2	3.185	6.12	16.3	2.087	0.520	−1.41	74.60
MoSe2	3.319	6.54	17.9	1.817	0.608	−10.45	93.25
WS2	3.180	6.14	14.6	2.250	0.351	15.72	213.46
WSe2	3.319	6.52	16.0	1.979	0.379	19.85	233.07

3. Results

Results of the calculations for three-particle states in MoS2, MoSe2, WS2, and WSe2 MLs is given in Figure 1, where we plot optical transition energies of trions (circle positions) and their oscillator strengths (circle size and color) as a function of the electron doping (the relative Fermi energy of the doping electrons). These are obtained by directly solving an effective three-particle Hamiltonian.

We distinguish two qualitatively different three-particle states: "trions", where both electrons are tightly bound, and "excitons", where one of the electrons is almost free, so that the state is close to being a two-particle exciton weakly coupled to a single electron [40,57,63]. The difference between excitons and trions is also clearly manifested in the doping dependence in Figure 1. It shows that the excitons' energy increases at larger doping, whereas, for tightly bound trions, the doping dependence is much weaker.

A tightly bound trion is the lowest-energy state. In WS2 and WSe2, this state is dark for all doping values, and in MoSe2, it is bright. The first optical transition due to the higher energy bright trion state is separated from the lowest one by a relatively large gap, $\Delta E \simeq 20$ meV, consistent with the GW-BSE approach for this energy difference [50].

On the contrary, MoS2 has four different but energetically closely spaced low-energy trion states, denoted T_1, T_2, T_3, and T_4, which give rise to transition energies within $\Delta E \simeq 2$ meV. Apart from the near-degeneracy, those trion states reveal another exciting feature: doping can change the brightness of the lowest energy state, which is dark at low doping values and brightens when doping increases. Doping also significantly changes the energy splitting of these states.

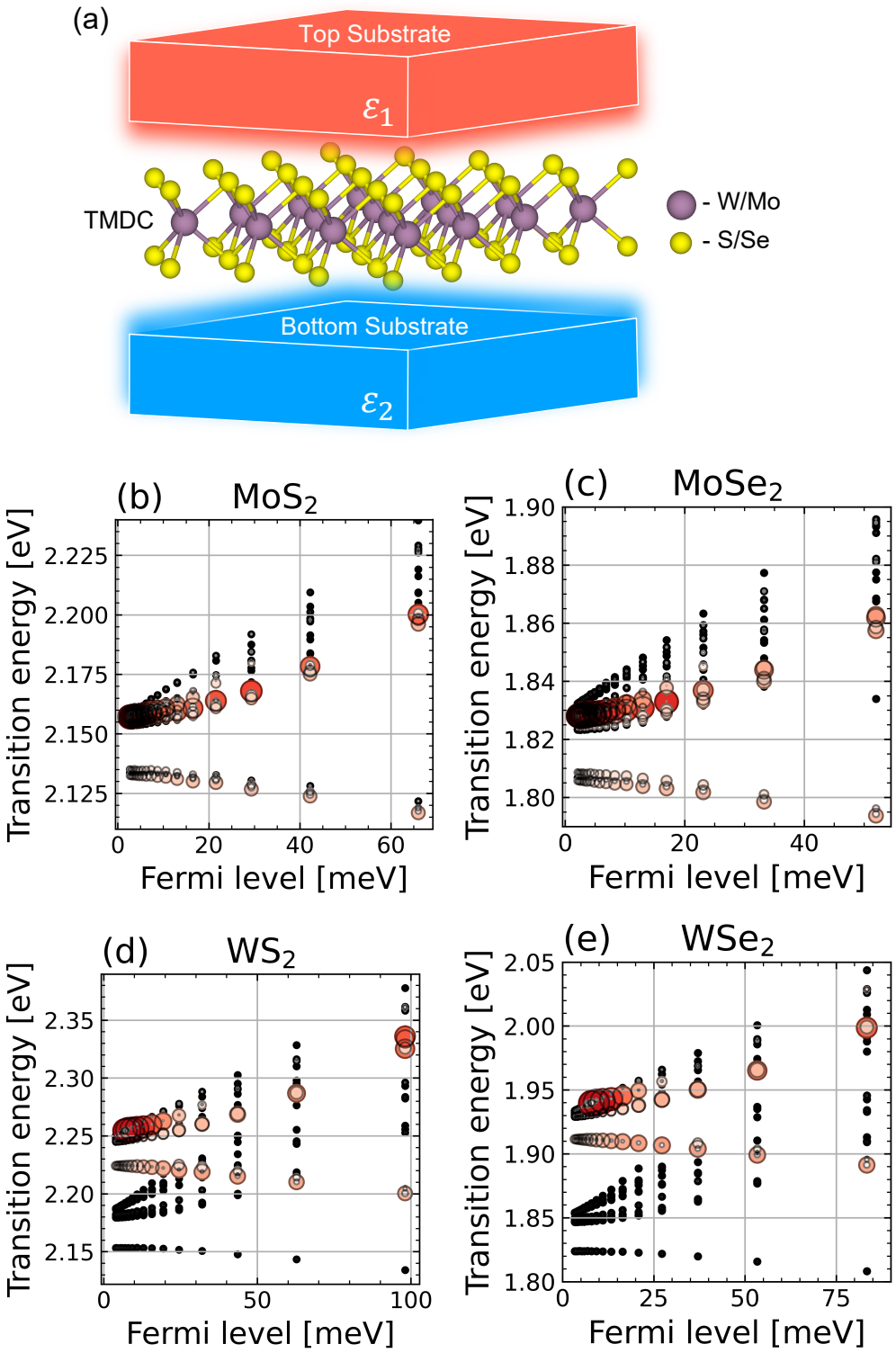

Figure 1. (**a**) Schematics of the TMDC monolayer placed between two dielectrics that define environmental screening $\varepsilon_{env} = (\varepsilon_1 + \varepsilon_2)/2$. (**b**–**e**) Energy diagram of the transition energies of the three-particle states calculated in freestanding ($\varepsilon_{env} = 1$) ML of MoS2 (**b**), MoSe2 (**c**), WS2 (**d**), and WSe2 (**e**) as a function of the Fermi level. Circle centers denote optical transition energies of trions. Colors and widths indicate their oscillator strengths (red) for bright states and (black) for dark ones. "Trion" and "exciton" denote trion and exciton states, depending on whether the second electron in the three-particle wavefunction is bound or not.

The fine structure and near degeneracy of these trion states in MoS2 ML is closely related to the spin-orbit coupling in the single-particle Hamiltonian, which appears in TMDCs due to the valley Zeeman splitting of the conduction band. At the same time, according to ab initio calculations, the Rashba coupling is minimal [58,59,61]. The calculations show that the Zeeman valley splitting is large in W-based materials [58,59,61]. Its value is reflected in the large gap between the lowest and the first excited bright trion states (Figure 1c,d). The splitting is also notable in the MoSe2 structure (Figure 1b). However, in the latter case, the splitting has a negative value, leading to a bright state of the lowest energy in MoSe2, unlike the W-based materials. In contrast, in MoS2, the valley Zeeman splitting is small, which is the main reason why the energies of the four lowest energies of the trion states are very similar.

4. Discussion

4.1. Symmetry and Internal Structure of Trions

The internal structure of trion states, particularly the weights of the contributions of the single-particle states, is the key to understanding their optical properties. Single-particle contributions (single-particle density matrix) for the T_1–T_4 trions, calculated for a freestanding MoS2 ML with the doping level of $E_F = 2.9$ meV, are illustrated in Figure 2. The figure shows single-particle bands for electrons (positive energies) and holes (negative energies) in the vicinity of the K and $-K$ valley points in the Brillouin zone. The blue and red denote the spin $s^z = \pm 1/2$ state. The center of a circle indicates the contribution of the single-particle state energy, whereas its radius indicates the contribution weight of this state to the trion wavefunction. Strong intervalley mixing by the Coulomb interaction creates a superposition of many single-particle states [42,65,66] so that a simple representation of trions as a product of a few states is generally impossible.

Note that trion states are classified by the valley quantum number $\tau = \tau_{c_1} + \tau_{c_2} - \tau_v$ and by the spin quantum number $s^z = s^z_{c_1} + s^z_{c_2} - s^z_v$ given as sums of the corresponding single particle numbers. We consider only states with $|\tau s^z| = 1/2$, which is a necessary (but not sufficient) condition for a state to be bright. The fine structure of $|\tau s^z| = 3/2$ states is discussed in Appendix C. If $|\tau s^z| \neq 1/2$, then the state does not have optically active electron-hole pairs contributing to the three-particle trion wavefunction. The T_1–T_4 states are split into qualitatively different pair states: T_1 and T_2 with $\tau s^z = 1/2$ and T_3 and T_4 with $\tau s^z = -1/2$.

The pair of trions T_3 and T_4 is a well-known singlet-triplet pair observed in earlier work [32,35,44,45,50,63,67–70], experimental and theoretical. In the T_1 and T_2 trion states, a hole is provided by a single valley ($-K$), while both valleys contribute electrons of different spin. In the vanishing doping limit, T_1 is dark and T_2 is bright because the valley electrons in these states have opposite spins [see Figure 2]. However, both the T_1 and T_2 states brighten as doping increases. At the same time, the T_3 and T_4 states comprise holes of opposite spins. In the limit of zero doping, T_4 is an optically parity forbidden state, while T_1 is an optically spin forbidden state. Notice that in addition to the T_1–T_4 trions, the system has four equivalent states, related by the symmetry transformation $K \leftrightarrow -K$.

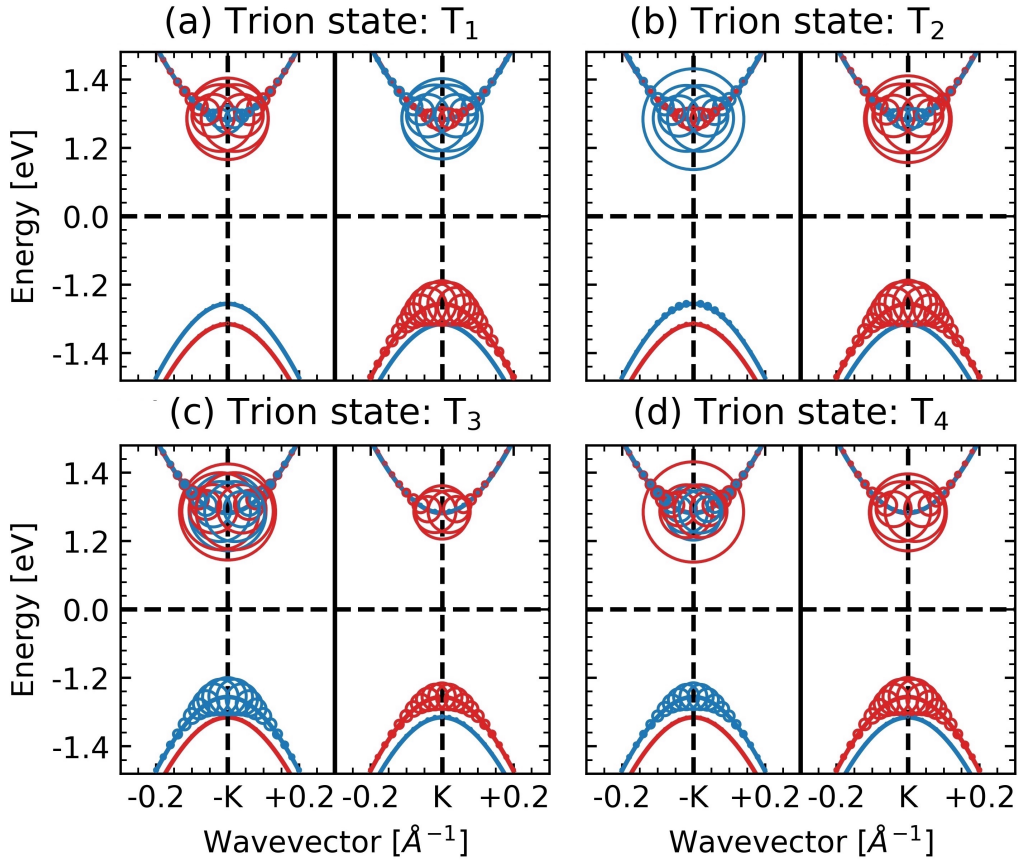

Figure 2. Contributions of Dirac single-particle band states in the vicinity of the K and $-K$ points to trions (panels (**a**–**d**)). A circle position points to the single-particle state and its radius gives weight to the exciton state; colors mark the spin projection s^z. The states T_1 and T_2 in panels (**a**,**b**) have $\tau s^z = 1/2$, and the states T_3 and T_4 in panels (**c**) and (**d**) have $\tau s^z = -1/2$. Results are shown for $E_F = 2.9$ meV.

4.2. Manipulating the Lowest Trion States

The near degeneracy of the trion states in MoS2 makes their energies and OS very sensitive to the parameters of the system, allowing a way to efficiently control the brightness of the lowest energy trion. In Figure 3a,b, we demonstrate anticrossing between the pairs of T_1–T_2 and T_3–T_4 states by subtracting the average values from their transition energies. One can see that the T_1 and T_3 states are the lowest energy states in the respective pairs, and the T_1 and T_4 states are dark at the zero doping limit, as shown in Figure 3c,d. The increase in doping brightens these initially dark states. Figure 3c shows that the oscillator strength of the T_1 state increases, whereas, for the T_2 state, it drops, such that the OSs of the two states become equal at $E_F \simeq 16$ meV. This interchange in brightness is accompanied by an energy change with the doping. The resulting behavior looks similar to a standard anti-crossing pattern, as seen in Figure 3a,b. The same brightness interchange and anticrossing is also observed for the other pair of states, T_2 and T_4. However, in this case, the anticrossing point is shifted to higher values of the doping level, that is, $E_F \simeq 50$ meV.

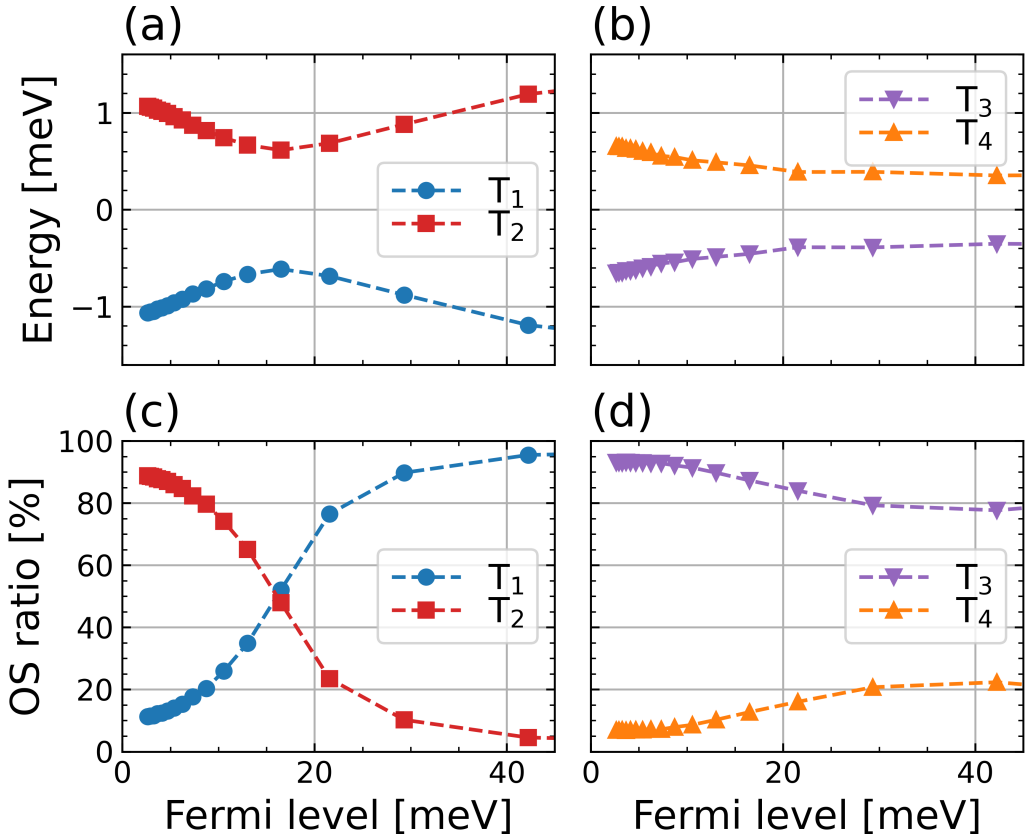

Figure 3. Doping dependence of relative transition energies of trion states T_1 and T_2 (**a**) and T_3 and T_4 (**b**) and relative oscillator strength of trion states T_1 and T_2 (**c**) and T_3 and T_4 (**d**) calculated for a free-standing MoS2 ML. The transition energies in (**a**,**b**) are shown with respect to their average at each doping level.

The fine structure of these trions can also be controlled by choosing the dielectric environment that embeds the ML. Figure 4 shows the color density plot for the oscillator strength ratio of the T_1 and T_2 states as a function of both the Fermi level E_F and the dielectric constant ε_{env}. The white dashed line in Figure 4 represents the anticrossing position corresponding to the doping level, where the oscillator strengths of both peaks are equal. One can see that, at vanishing doping, the lowest energy trion state is dark when $\varepsilon_{env} < 4$ and bright when $\varepsilon_{env} > 4$. This strong influence of the environment on the fine structure of the lowest-energy trion can, in principle, explain a discrepancy observed in different calculations and measurements with different conclusions on the brightness of the lowest-energy trion state in MoS2 [32,36,39,49,50]. Our calculations demonstrate that this discrepancy is due to the near-degeneracy, strong dependence on the environment, and influence of doping on the fine structure of the lowest-energy trion states. At the same time, we find that the environment has only a marginal effect on the states T_3 and T_4.

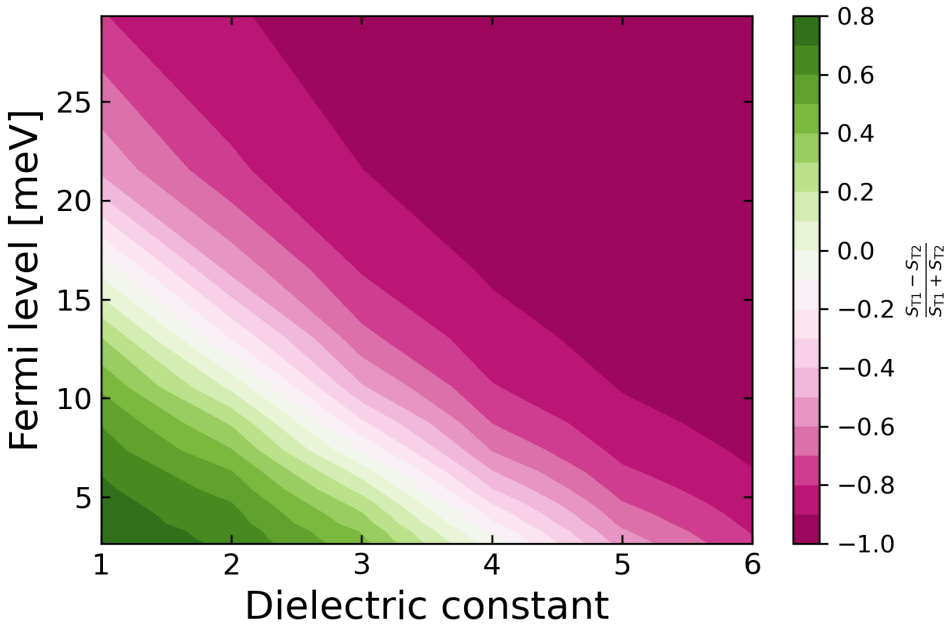

Figure 4. Dependence of the oscillator strength S_{T_1,T_2} of the T_1 and T_2 trion states on doping. The color scale shows the ratio $(S_{T_1} - S_{T_2})/(S_{T_1} + S_{T_2})$.

4.3. The Role of Spin-Orbit and Exchange Interactions

The fine structure of the trion states in MoS2 is defined by the small spin-orbit coupling and its interaction with the Coulomb exchange interaction, which determines the anticrossing mechanism in the trion states. To demonstrate this, we first note that despite a large admixture of many three-particle states, the pairs of states T_1–T_2 and T_3–T_4 are only weakly coupled to each other and other trion states of the higher energy. This fact is intuitive because these pairs have different values of $\tau s_z = \pm 1$ and therefore differ by their symmetry, which is also discussed in Reference [35]. At the same time, these states are practically uncoupled from the higher-energy states separated by a large gap [see Figure 1].

The interaction between trions is then pairwise and can then be modeled using a simple two-level effective Hamiltonian:

$$H = \begin{bmatrix} \epsilon_1 & g \\ g & \epsilon_2 \end{bmatrix}. \tag{4}$$

Here, diagonal elements comprise single- and many-body components $\epsilon_i = \langle i|H|i\rangle = \epsilon_i^{(0)} + \epsilon_i^{(1)}$, and their difference $\Delta = \epsilon_1 - \epsilon_2$ controls anticrossing.

For the pair T_1–T_2, a two-level basis is represented by the states $|1\rangle = |K_\downarrow, -K_\uparrow, -K_\downarrow\rangle$ (dark) and $|2\rangle = |K_\uparrow, -K_\downarrow, -K_\downarrow\rangle$ (bright). The single particle contribution to the energy difference $\Delta^{(0)} = 2\lambda_c$ follows from the spin-orbit splitting of the conduction band, whereas the many-body contribution $\Delta^{(1)} \simeq V^{cv}_{\text{exc}}(K=0) > 0$ is defined mainly by the intravalley electron-hole exchange interaction. The off-diagonal coupling elements $g = W^{cc}_{\text{exc}}(K) < 0$ are defined by the intervalley electron-electron exchange interaction, which is a few meV [66]. The anticrossing condition for this pair $\Delta_{T_1-T_2} \simeq 2\lambda_c + V^{cv}_{\text{exc}}(K=0) = 0$ can be satisfied when λ_c is relatively small and negative, and this indeed occurs in MoS2.

At the same time, the basis for the T_3 and T_4 states is represented by $|1\rangle = |K_\downarrow, K_\uparrow, K_\uparrow\rangle$ (bright) and $|2\rangle = |K_\downarrow, -K_\downarrow, -K_\downarrow\rangle$ (bright). The energy difference $\Delta_{T_3-T_4} = \epsilon_1 - \epsilon_2 = \epsilon_1^{(1)} = W^{cc}_{\text{dir}}(K=0) > 0$ between the diagonal elements is mainly defined by the direct electron-electron intravalley interaction, which is the many-body component of the diagonal energy of the state $|1\rangle$. The single-particle contributions in both states are the same and

yield zero difference. The off-diagonal coupling in this case $g = V_{\text{exc}}^{cv}(K) > 0$ is obtained by hopping electron-hole intervalley pairs due to the intervalley electron-hole exchange interaction [71–73]. In the zero doping level limit, the interaction between the T_3 and T_4 trions leads to the T_4 state becoming optically forbidden. In contrast to the T_1–T_2 pair, the T_3–T_4 trion pair has strong off-diagonal coupling in all TMDC monolayers, whereas the diagonal energy difference $\Delta_{T_3-T_4}$ does not depend on λ_c and is practically identical for all TMDCs. In all TMDC monolayers, the pair T_1–T_2 yields the lowest energy ground state. This implies that the ground state of the trion can be efficiently controlled by the doping and dielectric environment only in the MoS2 monolayers.

5. Conclusions

The analysis of three-particle states in TMDC MLs, based on a direct diagonalization of the corresponding Hamiltonian, classifies the low-energy trion states' fine structure and spectral properties of doped TMDCs. In particular, we demonstrate the bright-dark interchange of the lowest-energy trions as a function of doping and the dielectric environment. The calculations reveal that the energies and oscillator strengths of the lowest-energy trion states are defined mainly by the spin-orbit coupling and its interplay with the exchange interaction. When those quantities are similar, a material can exhibit a near-degeneracy of its four lowest-energy trion states, making them sensitive to the system parameters. This sensitivity opens the possibility of manipulating the position and brightness of the lowest-energy trion and thus the low-energy spectrum, simply by changing the electrostatic doping and choosing the dielectric environment. In particular, this situation can easily be realized in MoS2, where the sensitivity of the fine structure of the trion explains the origin of the controversy about whether the lowest trion energy is bright or dark. On the basis of the interplay between the fine-structure splitting and many-body effects, the controlling mechanism is generic and applies to other similar structures. Our results explain existing experimental observations of trion states in 2D multivalley materials and open new perspectives for their optoelectronic applications.

Author Contributions: Y.V.Z. performed numerical calculations of trion spectra, with contributions from D.R.G., V.P., A.V. and D.R.G. supervised the project. A.V. and V.P. wrote the manuscript, with crucial contributions from all authors. All authors have read and agreed to the published version of the manuscript.

Funding: We acknowledge support from the Russian Science Foundation under grant 18-12-00429, used for numerical calculations. Y. V. Z is grateful to the Deutsche Forschungsgemeinschaft (DFG, German Research Foundation) SPP 2244 (Project ID 443416183) for financial support. A.V. is grateful for support from the HSE University Basic Research Program used to compile the results and write the manuscript. V. P. acknowledges funding from the Vice President for Research and Economic Development (VPRED), SUNY Research Seed Grant Program, and computational facilities at the Center for Computational Research at the University at Buffalo (http://hdl.handle.net/10477/79221, accessed on 27 September 2022).

Institutional Review Board Statement: Not applicable.

Informed Consent Statement: Not applicable.

Data Availability Statement: The data that support the findings of this study are available from the corresponding authors upon reasonable request.

Conflicts of Interest: The authors declare no conflict of interest.

Abbreviations

The following abbreviations are used in this manuscript:

ML	monolayers
TMDC	transitional metal dichalcogenides

2D	two-dimensional
DFT	density functional theory
GW	GW approximation

Appendix A. Computational Details: Single-Particle States

Trion states in a doped monolayer TDMC are calculated by solving an eigenvalue problem for the Hamiltonian for trion states constructed using a basis set of single-particle states in the valence and conduction bands. The doping influence is taken into account by connecting the discretization of the Brillouin zone with the doping-induced Pauli blocking [57]. We used the observation that the lowest energy trion states in TMDC monolayers are created from the single-particle states in the vicinity of points K and $K' = -K$ of the Brillouin zone [36,57]. These states are well described by the massive Dirac Hamiltonian model in Equation (3).

We consider that the monolayer is embedded in a dielectric environment, with dielectric constants $\varepsilon_{1,2}$ for material on both sides of the monolayer. The environment affects the energy gap Δ, which can be expressed using an analytical formula [56]

$$\Delta = \Delta_0 + \frac{e^2}{2\varepsilon d}\left[\frac{L_2 + L_1}{\sqrt{L_2 L_1}}\tanh^{-1}(\sqrt{L_2 L_1}) - \ln(1 - L_2 L_1)\right], \quad L_i = \frac{\varepsilon - \varepsilon_i}{\varepsilon + \varepsilon_i}, \tag{A1}$$

where ε is the dielectric constant of the bulk TMDC, d is the thickness of the monolayer and Δ_0 are the bare values of the gap.

Appendix B. Trion States

Quantum states T of negatively charged trions (two electrons and one hole) are obtained by solving the three-body eigenvalue problem derived by spanning the full many-body Hamiltonian onto the space of trion states constructed as a linear superposition

$$|T\rangle = \sum_{c_1,c_2,v} A^T_{c_1c_2v}|c_1c_2v\rangle, \; |c_1c_2v\rangle = a^\dagger_{c_1}a^\dagger_{c_2}a^\dagger_v|0\rangle, \tag{A2}$$

where $c_{1,2}$ denote electron states in the conduction band, v are hole states in the valence band, and the ground state $|0\rangle$ has a filled valence band and an empty conduction band. Double counting is avoided by imposing the restriction $c_1 < c_2$. The corresponding three-particle wavefunction is constructed from the single-particle functions $\phi_{c,v}(x)$ as

$$\Psi^T(x_1, x_2, x_3) = \frac{1}{\sqrt{2}}\sum_{c_1,c_2,v} A^T_{c_1c_2v}\phi^*_v(x_3) \times \left[\phi_{c_1}(x_1)\phi_{c_2}(x_2) - \phi_{c_2}(x_1)\phi_{c_1}(x_2)\right]. \tag{A3}$$

Both the electron and hole parts of the trion state are antisymmetric, which is reflected in the direct- and exchange-interaction potentials between electrons and holes. The representation of the wave function does not require explicit antisymmetrization between holes and electrons [74], which follows from a direct calculation of the wave function of excitons [75].

Coefficients $A^T_{c_1c_2v}$ in Equation (A2) are found by solving the matrix eigenvalue problem.

$$\sum_{c_1'c_2'v'} H^{c_1'c_2'v'}_{c_1c_2v} A^T_{c_1'c_2'v'} = E_t A^T_{c_1c_2v}. \tag{A4}$$

The Hamiltonian matrix $H = H_0 + H_{cc} + H_{cv}$ comprises three contributions:

$$H_0 = (\varepsilon_{c_1} + \varepsilon_{c_2} - \varepsilon_v)\delta_{c_1c_1'}\delta_{c_2c_2'}\delta_{vv'},$$
$$H_{cc} = (W^{c_1'c_2'}_{c_1c_2} - W^{c_2'c_1'}_{c_1c_2})\delta_{vv'},$$
$$H_{cv} = -(W^{vc_1'}_{v'c_1} - V^{c_1'v}_{v'c_1})\delta_{c_2c_2'} - (W^{vc_2'}_{v'c_2} - V^{c_2'v}_{v'c_2})\delta_{c_1c_1'} + (W^{vc_2'}_{v'c_1} - V^{c_2'v}_{v'c_1})\delta_{c_2c_1'} + (W^{vc_1'}_{v'c_2} - V^{c_1'v}_{v'c_2})\delta_{c_1c_2'},$$

where $\varepsilon_{c,v}$ denote the energy of the single-particle particle states, W and V are the screened and bare Coulomb matrix elements, respectively. This approach is a direct extension of the Tamm-Dancoff approximation for two-particle excitons onto three-particle trions. Matrix elements for the bare Coulomb interaction are given by

$$V_{cd}^{ab} = V(\mathbf{k}_a - \mathbf{k}_c)\langle u_c|u_a\rangle\langle u_d|u_b\rangle, \tag{A5}$$

where $V(q) = 2\pi e^2/q$ is the Fourier component of the bare Coulomb potential and $\langle u_c|u_a\rangle$ is the overlap of the single-particle Bloch states c and a. The screened potential has a similar form to Equation (A5), however, instead of the bare Coulomb potential $V(q)$ one uses the standard Rytova-Keldysh potential [52–54] given in Equation (2). Note that the screening depends on the geometry of the device. In particular, it is modified when the vacuum spacing appears between the monolayer and the dielectric environment [55]. However, in this work, this effect is neglected.

Symmetries of the three-particle Hamiltonian give rise to several conserved quantities, which helps to reduce the numerical efforts. These include the total trion momentum $\mathbf{k} = \mathbf{k}_{c_1} + \mathbf{k}_{c_2} - \mathbf{k}_v$ and z axis spin projection $s^z = s^z_{c_1} + s^z_{c_2} - s^z_v$. Furthermore, the analysis is restricted to trions with total spin $1/2$, since only such states are optically active. Therefore, we neglect the states with spin $3/2$ in the main text and consider them in the following.

The trion states are classified by the z component of the electron spin, $s^z_{c_1} + s^z_{c_2} = 1$ and 0 [35,39,63,76,77], and distinguish between the intra- and inter-valley trion states by the quantities $\tau_{c_1} + \tau_{c_2} = 2$ and 0, respectively [39,63]. The trion states can also be classified by the product $s_z\tau$ of the total spin projection s^z and the total valley index $\tau = \tau_{c_1} + \tau_{c_2} - \tau_v$. A necessary (but not sufficient) condition for a state to be bright is $s^z\tau = \pm 1/2$.

Finally, the influence of electron doping is taken into account by using the approach described in Ref. [57], where the Pauli blocking of the occupied electron states is modeled by choosing the discretized mesh with the interval δK in the Brillouin zone. The doping density $n = g_v g_s/(\Omega_0 N^2)$ is related to the number of mesh points $N \times N$ and the area of the primitive cell Ω_0 (g_s and g_v are spin and valley degeneracies, respectively). The corresponding Fermi energy of the doping electrons is given by $E_F = \hbar^2\delta k^2/2m$ where the discretization interval for the hexagonal lattice of MoS2 is $\delta k = 4\pi/(\sqrt{3}aN)$.

Appendix C. Trion $s^z\tau = \pm 3/2$ States

The trion states $s^z\tau = \pm 3/2$ are fully dark and scattering between $s^z\tau = \pm 3/2$ and $s^z\tau = \pm 1/2$ requires a nonzero spin-boson. However, in the presence of an intersystem crossing from singlet to triplet excitons, it is possible to obtain the $s^z\tau = \pm 3/2$ trion state in the freestanding of the MoS2 monolayer as the lowest trion states, with significant changes in the photoluminescence temperature dependence. The energy splitting between the lowest $s^z\tau = \pm 3/2$ state and the lowest $s^z\tau = \pm 1/2$ state will be about 2.3 meV in the zero doping level limit, as shown in Figure A1a. This effect is due to the absence of repulsive exchange interaction between the hole and electrons, see Figure A1b, and will also be observed only in the MoS2 monolayer due to the low conduction band splitting, which is comparable to the amplitude of the exchange interaction.

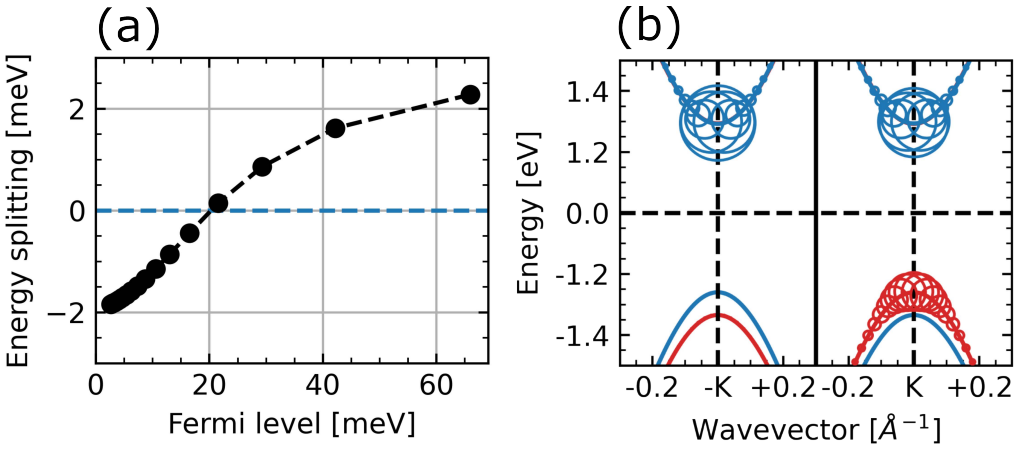

Figure A1. (**a**) Trion energy splitting between the lowest $s^z\tau = \pm 3/2$ state and the lowest $s^z\tau = \pm 1/2$ states of the freestanding of MoS2 monolayer. For a wide range of doping, the fully dark $s^z\tau = \pm 3/2$ state will be the lowest trion state of the freestanding of MoS2 monolayer. (**b**) Contributions of the Dirac single-particle band states in the vicinity of the K and $-K$ points to the lowest $s^z\tau = \pm 3/2$ trion state.

References

1. Mak, K.F.; Lee, C.; Hone, J.; Shan, J.; Heinz, T.F. Atomically Thin MoS_2: A New Direct-Gap Semiconductor. *Phys. Rev. Lett.* **2010**, *105*, 136805. [CrossRef] [PubMed]
2. Splendiani, A.; Sun, L.; Zhang, Y.; Li, T.; Kim, J.; Chim, C.Y.; Galli, G.; Wang, F. Emerging Photoluminescence in Monolayer MoS_2. *Nano Lett.* **2010**, *10*, 1271–1275. [CrossRef] [PubMed]
3. Komsa, H.P.; Krasheninnikov, A.V. Effects of confinement and environment on the electronic structure and exciton binding energy of MoS_2 from first principles. *Phys. Rev. B* **2012**, *86*, 241201. [CrossRef]
4. Feng, J.; Qian, X.; Huang, C.W.; Li, J. Strain-engineered artificial atom as a broad-spectrum solar energy funnel. *Nat. Photonics* **2012**, *6*, 866–872. [CrossRef]
5. Qiu, D.Y.; da Jornada, F.H.; Louie, S.G. Optical Spectrum of MoS_2: Many-Body Effects and Diversity of Exciton States. *Phys. Rev. Lett.* **2013**, *111*, 216805. [CrossRef]
6. Amara, I.B.; Salem, E.B.; Jaziri, S. Optoelectronic response and excitonic properties of monolayer MoS_2. *J. Appl. Phys.* **2016**, *120*, 051707. [CrossRef]
7. Muth, J.F.; Lee, J.H.; Shmagin, I.K.; Kolbas, R.M.; Casey, H.C.; Keller, B.P.; Mishra, U.K.; DenBaars, S.P. Absorption coefficient, energy gap, exciton binding energy, and recombination lifetime of GaN obtained from transmission measurements. *Appl. Phys. Lett.* **1997**, *71*, 2572–2574. [CrossRef]
8. Yu, P.Y.; Cardona, M. *Fundamentals of Semiconductors*; Springer: Berlin/Heidelberg, Germany, 2010. [CrossRef]
9. Dvorak, M.; Wei, S.H.; Wu, Z. Origin of the Variation of Exciton Binding Energy in Semiconductors. *Phys. Rev. Lett.* **2013**, *110*, 016402. [CrossRef]
10. Mak, K.F.; He, K.; Lee, C.; Lee, G.H.; Hone, J.; Heinz, T.F.; Shan, J. Tightly bound trions in monolayer MoS_2. *Nat. Mater.* **2012**, *12*, 207–211. [CrossRef]
11. Mouri, S.; Miyauchi, Y.; Matsuda, K. Tunable Photoluminescence of Monolayer MoS_2 via Chemical Doping. *Nano Lett.* **2013**, *13*, 5944–5948. [CrossRef]
12. Ross, J.S.; Klement, P.; Jones, A.M.; Ghimire, N.J.; Yan, J.; Mandrus, D.G.; Taniguchi, T.; Watanabe, K.; Kitamura, K.; Yao, W.; et al. Electrically tunable excitonic light-emitting diodes based on monolayer WSe_2 p–n junctions. *Nat. Nanotechnol.* **2014**, *9*, 268–272. [CrossRef] [PubMed]
13. Lui, C.; Frenzel, A.; Pilon, D.; Lee, Y.H.; Ling, X.; Akselrod, G.; Kong, J.; Gedik, N. Trion-Induced Negative Photoconductivity in Monolayer MoS_2. *Phys. Rev. Lett.* **2014**, *113*, 166801. [CrossRef] [PubMed]
14. Zhang, C.; Wang, H.; Chan, W.; Manolatou, C.; Rana, F. Absorption of light by excitons and trions in monolayers of metal dichalcogenide MoS_2: Experiments and theory. *Phys. Rev. B* **2014**, *89*, 205436. [CrossRef]
15. Scheuschner, N.; Ochedowski, O.; Kaulitz, A.M.; Gillen, R.; Schleberger, M.; Maultzsch, J. Photoluminescence of freestanding single- and few-layer MoS_2. *Phys. Rev. B* **2014**, *89*, 125406. [CrossRef]
16. Soklaski, R.; Liang, Y.; Yang, L. Temperature effect on optical spectra of monolayer molybdenum disulfide. *Appl. Phys. Lett.* **2014**, *104*, 193110. [CrossRef]
17. Zhang, Y.; Li, H.; Wang, H.; Liu, R.; Zhang, S.L.; Qiu, Z.J. On Valence-Band Splitting in Layered MoS_2. *ACS Nano* **2015**, *9*, 8514–8519. [CrossRef]
18. Rezk, A.R.; Carey, B.; Chrimes, A.F.; Lau, D.W.M.; Gibson, B.C.; Zheng, C.; Fuhrer, M.S.; Yeo, L.Y.; Kalantar-zadeh, K. Acoustically-Driven Trion and Exciton Modulation in Piezoelectric Two-Dimensional MoS_2. *Nano Lett.* **2016**, *16*, 849–855. [CrossRef]

19. Singh, A.; Moody, G.; Tran, K.; Scott, M.E.; Overbeck, V.; Berghäuser, G.; Schaibley, J.; Seifert, E.J.; Pleskot, D.; Gabor, N.M.; et al. Trion formation dynamics in monolayer transition metal dichalcogenides. *Phys. Rev. B* **2016**, *93*, 041401. [CrossRef]
20. You, Y.; Zhang, X.X.; Berkelbach, T.C.; Hybertsen, M.S.; Reichman, D.R.; Heinz, T.F. Observation of biexcitons in monolayer WSe2. *Nat. Phys.* **2015**, *11*, 477–481. [CrossRef]
21. Sie, E.J.; Frenzel, A.J.; Lee, Y.H.; Kong, J.; Gedik, N. Intervalley biexcitons and many-body effects in monolayer MoS2. *Phys. Rev. B* **2015**, *92*, 125417. [CrossRef]
22. Plechinger, G.; Nagler, P.; Kraus, J.; Paradiso, N.; Strunk, C.; Schüller, C.; Korn, T. Identification of excitons, trions and biexcitons in single-layer WS2. *Phys. Status Solidi* **2015**, *9*, 457–461. [CrossRef]
23. Hao, K.; Specht, J.F.; Nagler, P.; Xu, L.; Tran, K.; Singh, A.; Dass, C.K.; Schüller, C.; Korn, T.; Richter, M.; et al. Neutral and charged inter-valley biexcitons in monolayer MoSe2. *Nat. Commun.* **2017**, *8*, 15552. [CrossRef] [PubMed]
24. Paradisanos, I.; Germanis, S.; Pelekanos, N.T.; Fotakis, C.; Kymakis, E.; Kioseoglou, G.; Stratakis, E. Room temperature observation of biexcitons in exfoliated WS2 monolayers. *Appl. Phys. Lett.* **2017**, *110*, 193102. [CrossRef]
25. Ye, Z.; Waldecker, L.; Ma, E.Y.; Rhodes, D.; Antony, A.; Kim, B.; Zhang, X.X.; Deng, M.; Jiang, Y.; Lu, Z.; et al. Efficient generation of neutral and charged biexcitons in encapsulated WSe2 monolayers. *Nat. Commun.* **2018**, *9*, 3718. [CrossRef] [PubMed]
26. Torche, A.; Bester, G. Biexcitons fine structure and non-equilibrium effects in transition metal dichalcogenides monolayers from first principles. *Commun. Phys.* **2021**, *4*, 67. [CrossRef]
27. Gmitra, M.; Fabian, J. Proximity Effects in Bilayer Graphene on Monolayer WSe2: Field-Effect Spin Valley Locking, Spin-Orbit Valve, and Spin Transistor. *Phys. Rev. Lett.* **2017**, *119*, 146401. [CrossRef]
28. Ciccarino, C.J.; Christensen, T.; Sundararaman, R.; Narang, P. Dynamics and Spin-Valley Locking Effects in Monolayer Transition Metal Dichalcogenides. *Nano Lett.* **2018**, *18*, 5709–5715. [CrossRef]
29. Tao, L.L.; Tsymbal, E.Y. Two-dimensional spin-valley locking spin valve. *Phys. Rev. B* **2019**, *100*, 161110(R). [CrossRef]
30. Wang, Y.; Deng, L.; Wei, Q.; Wan, Y.; Liu, Z.; Lu, X.; Li, Y.; Bi, L.; Zhang, L.; Lu, H.; et al. Spin-Valley Locking Effect in Defect States of Monolayer MoS2. *Nano Lett.* **2020**, *20*, 2129–2136. [CrossRef]
31. Ganchev, B.; Drummond, N.; Aleiner, I.; Fal'ko, V. Three-Particle Complexes in Two-Dimensional Semiconductors. *Phys. Rev. Lett.* **2015**, *114*, 107401. [CrossRef]
32. Plechinger, G.; Nagler, P.; Arora, A.; Schmidt, R.; Chernikov, A.; del Águila, A.G.; Christianen, P.C.; Bratschitsch, R.; Schüller, C.; Korn, T. Trion fine structure and coupled spin–valley dynamics in monolayer tungsten disulfide. *Nat. Commun.* **2016**, *7*, 12715. [CrossRef] [PubMed]
33. Efimkin, D.K.; MacDonald, A.H. Many-body theory of trion absorption features in two-dimensional semiconductors. *Phys. Rev. B* **2017**, *95*, 035417. [CrossRef]
34. Mostaani, E.; Szyniszewski, M.; Price, C.H.; Maezono, R.; Danovich, M.; Hunt, R.J.; Drummond, N.D.; Fal'ko, V.I. Diffusion quantum Monte Carlo study of excitonic complexes in two-dimensional transition-metal dichalcogenides. *Phys. Rev. B* **2017**, *96*, 075431. [CrossRef]
35. Courtade, E.; Semina, M.; Manca, M.; Glazov, M.M.; Robert, C.; Cadiz, F.; Wang, G.; Taniguchi, T.; Watanabe, K.; Pierre, M.; et al. Charged excitons in monolayer WSe2: Experiment and theory. *Phys. Rev. B* **2017**, *96*, 085302. [CrossRef]
36. Drüppel, M.; Deilmann, T.; Krüger, P.; Rohlfing, M. Diversity of trion states and substrate effects in the optical properties of an MoS_2 monolayer. *Nat. Commun.* **2017**, *8*, 2117. [CrossRef]
37. Wang, G.; Chernikov, A.; Glazov, M.M.; Heinz, T.F.; Marie, X.; Amand, T.; Urbaszek, B. Colloquium: Excitons in atomically thin transition metal dichalcogenides. *Rev. Mod. Phys.* **2018**, *90*, 021001. [CrossRef]
38. Arora, A.; Deilmann, T.; Reichenauer, T.; Kern, J.; Michaelis de Vasconcellos, S.; Rohlfing, M.; Bratschitsch, R. Excited-State Trions in Monolayer WS_2. *Phys. Rev. Lett.* **2019**, *123*, 167401. [CrossRef]
39. Torche, A.; Bester, G. First-principles many-body theory for charged and neutral excitations: Trion fine structure splitting in transition metal dichalcogenides. *Phys. Rev. B* **2019**, *100*, 201403. [CrossRef]
40. Zhumagulov, Y.V.; Vagov, A.; Gulevich, D.R.; Junior, P.E.F.; Perebeinos, V. Trion induced photoluminescence of a doped MoS2 monolayer. *J. Chem. Phys.* **2020**, *153*, 044132. [CrossRef]
41. Hichri, A.; Jaziri, S. Trion fine structure and anomalous Hall effect in monolayer transition metal dichalcogenides. *Phys. Rev. B* **2020**, *102*, 085407. [CrossRef]
42. Grzeszczyk, M.; Olkowska-Pucko, K.; Nogajewski, K.; Watanabe, K.; Taniguchi, T.; Kossacki, P.; Babiński, A.; Molas, M.R. Exposing the trion's fine structure by controlling the carrier concentration in hBN-encapsulated MoS2. *Nanoscale* **2021**, *13*, 18726–18733. [CrossRef] [PubMed]
43. Jadczak, J.; Kutrowska-Girzycka, J.; Bieniek, M.; Kazimierczuk, T.; Kossacki, P.; Schindler, J.J.; Debus, J.; Watanabe, K.; Taniguchi, T.; Ho, C.H.; et al. Probing negatively charged and neutral excitons in MoS2/hBN and hBN/MoS2/hBN van der Waals heterostructures. *Nanotechnology* **2021**, *32*, 145717. [CrossRef] [PubMed]
44. Zinkiewicz, M.; Woźniak, T.; Kazimierczuk, T.; Kapuscinski, P.; Oreszczuk, K.; Grzeszczyk, M.; Bartoš, M.; Nogajewski, K.; Watanabe, K.; Taniguchi, T.; et al. Excitonic Complexes in n-Doped WS2 Monolayer. *Nano Lett.* **2021**, *21*, 2519–2525. [CrossRef] [PubMed]
45. Chang, Y.W.; Chang, Y.C. Variationally optimized orbital approach to trions in two-dimensional materials. *J. Chem. Phys.* **2021**, *155*, 024110. [CrossRef] [PubMed]
46. Hamby, D.W.; Lucca, D.A.; Klopfstein, M.J.; Cantwell, G. Temperature dependent exciton photoluminescence of bulk ZnO. *J. Appl. Phys.* **2003**, *93*, 3214–3217. [CrossRef]

47. Amori, A.R.; Rossi, J.E.; Landi, B.J.; Krauss, T.D. Defects Enable Dark Exciton Photoluminescence in Single-Walled Carbon Nanotubes. *J. Phys. Chem. C* **2018**, *122*, 3599–3607. [CrossRef]
48. Golovynskyi, S.; Bosi, M.; Seravalli, L.; Li, B. MoS2 two-dimensional quantum dots with weak lateral quantum confinement: Intense exciton and trion photoluminescence. *Surfaces Interfaces* **2021**, *23*, 100909. [CrossRef]
49. Deilmann, T.; Thygesen, K.S. Dark excitations in monolayer transition metal dichalcogenides. *Phys. Rev. B* **2017**, *96*, 201113. [CrossRef]
50. Arora, A.; Wessling, N.K.; Deilmann, T.; Reichenauer, T.; Steeger, P.; Kossacki, P.; Potemski, M.; de Vasconcellos, S.M.; Rohlfing, M.; Bratschitsch, R. Dark trions govern the temperature-dependent optical absorption and emission of doped atomically thin semiconductors. *Phys. Rev. B* **2020**, *101*, 241413(R). [CrossRef]
51. Berkelbach, T.C.; Hybertsen, M.S.; Reichman, D.R. Theory of neutral and charged excitons in monolayer transition metal dichalcogenides. *Phys. Rev. B* **2013**, *88*, 045318. [CrossRef]
52. Rytova, N.S. The screened potential of a point charge in a thin film. *Mosc. Univ. Phys. Bull.* **1967**, *3*, 18.
53. Keldysh, L.V. Coulomb interaction in thin semiconductor and semimetal films. *Sov. J. Exp. Theor. Phys. Lett.* **1979**, *29*, 658.
54. Cudazzo, P.; Tokatly, I.V.; Rubio, A. Dielectric screening in two-dimensional insulators: Implications for excitonic and impurity states in graphane. *Phys. Rev. B* **2011**, *84*, 085406. [CrossRef]
55. Florian, M.; Hartmann, M.; Steinhoff, A.; Klein, J.; Holleitner, A.W.; Finley, J.J.; Wehling, T.O.; Kaniber, M.; Gies, C. The Dielectric Impact of Layer Distances on Exciton and Trion Binding Energies in van der Waals Heterostructures. *Nano Lett.* **2018**, *18*, 2725–2732. [CrossRef] [PubMed]
56. Cho, Y.; Berkelbach, T.C. Environmentally sensitive theory of electronic and optical transitions in atomically thin semiconductors. *Phys. Rev. B* **2018**, *97*, 041409(R). [CrossRef]
57. Zhumagulov, Y.V.; Vagov, A.; Senkevich, N.Y.; Gulevich, D.R.; Perebeinos, V. Three-particle states and brightening of intervalley excitons in a doped MoS2 monolayer. *Phys. Rev. B* **2020**, *101*, 245433. [CrossRef]
58. Xiao, D.; Liu, G.B.; Feng, W.; Xu, X.; Yao, W. Coupled Spin and Valley Physics in Monolayers of MoS_2 and Other Group-VI Dichalcogenides. *Phys. Rev. Lett.* **2012**, *108*, 196802. [CrossRef]
59. Kormányos, A.; Burkard, G.; Gmitra, M.; Fabian, J.; Zólyomi, V.; Drummond, N.D.; Fal'ko, V. k·ptheory for two-dimensional transition metal dichalcogenide semiconductors. *2D Mater.* **2015**, *2*, 022001. [CrossRef]
60. Zhang, C.; Gong, C.; Nie, Y.; Min, K.A.; Liang, C.; Oh, Y.J.; Zhang, H.; Wang, W.; Hong, S.; Colombo, L.; et al. Systematic study of electronic structure and band alignment of monolayer transition metal dichalcogenides in Van der Waals heterostructures. *2D Mater.* **2016**, *4*, 015026. [CrossRef]
61. Zollner, K.; Junior, P.E.F.; Fabian, J. Strain-tunable orbital, spin-orbit, and optical properties of monolayer transition-metal dichalcogenides. *Phys. Rev. B* **2019**, *100*, 195126. [CrossRef]
62. Waldecker, L.; Raja, A.; Rösner, M.; Steinke, C.; Bostwick, A.; Koch, R.J.; Jozwiak, C.; Taniguchi, T.; Watanabe, K.; Rotenberg, E.; et al. Rigid Band Shifts in Two-Dimensional Semiconductors through External Dielectric Screening. *Phys. Rev. Lett.* **2019**, *123*, 206403. [CrossRef] [PubMed]
63. Tempelaar, R.; Berkelbach, T.C. Many-body simulation of two-dimensional electronic spectroscopy of excitons and trions in monolayer transition metal dichalcogenides. *Nat. Commun.* **2019**, *10*, 3419. [CrossRef] [PubMed]
64. Laturia, A.; de Put, M.L.V.; Vandenberghe, W.G. Dielectric properties of hexagonal boron nitride and transition metal dichalcogenides: from monolayer to bulk. *NPJ 2D Mater. Appl.* **2018**, *2*, 6. [CrossRef]
65. Klein, J.; Hötger, A.; Florian, M.; Steinhoff, A.; Delhomme, A.; Taniguchi, T.; Watanabe, K.; Jahnke, F.; Holleitner, A.W.; Potemski, M.; et al. Controlling exciton many-body states by the electric-field effect in monolayer MoS_2. *Phys. Rev. Res.* **2021**, *3*, L022009. [CrossRef]
66. Danovich, M.; Zólyomi, V.; Fal'ko, V.I. Dark trions and biexcitons in WS2 and WSe2 made bright by e-e scattering. *Sci. Rep.* **2017**, *7*, 45998. [CrossRef]
67. Vaclavkova, D.; Wyzula, J.; Nogajewski, K.; Bartos, M.; Slobodeniuk, A.O.; Faugeras, C.; Potemski, M.; Molas, M.R. Singlet and triplet trions in WS2 monolayer encapsulated in hexagonal boron nitride. *Nanotechnology* **2018**, *29*, 325705. [CrossRef]
68. Zipfel, J.; Wagner, K.; Ziegler, J.D.; Taniguchi, T.; Watanabe, K.; Semina, M.A.; Chernikov, A. Light–matter coupling and non-equilibrium dynamics of exchange-split trions in monolayer WS2. *J. Chem. Phys.* **2020**, *153*, 034706. [CrossRef]
69. Plechinger, G.; Nagler, P.; Arora, A.; del Águila, A.G.; Ballottin, M.V.; Frank, T.; Steinleitner, P.; Gmitra, M.; Fabian, J.; Christianen, P.C.M.; et al. Excitonic Valley Effects in Monolayer WS2 under High Magnetic Fields. *Nano Lett.* **2016**, *16*, 7899–7904. [CrossRef]
70. Fu, J.; Cruz, J.M.R.; Qu, F. Valley dynamics of different trion species in monolayer WSe2. *Appl. Phys. Lett.* **2019**, *115*, 082101. [CrossRef]
71. Glazov, M.M.; Amand, T.; Marie, X.; Lagarde, D.; Bouet, L.; Urbaszek, B. Exciton fine structure and spin decoherence in monolayers of transition metal dichalcogenides. *Phys. Rev. B* **2014**, *89*, 201302. [CrossRef]
72. Selig, M.; Katsch, F.; Schmidt, R.; Michaelis de Vasconcellos, S.; Bratschitsch, R.; Malic, E.; Knorr, A. Ultrafast dynamics in monolayer transition metal dichalcogenides: Interplay of dark excitons, phonons, and intervalley exchange. *Phys. Rev. Res.* **2019**, *1*, 022007. [CrossRef]
73. Qiu, D.Y.; Cao, T.; Louie, S.G. Nonanalyticity, Valley Quantum Phases, and Lightlike Exciton Dispersion in Monolayer Transition Metal Dichalcogenides: Theory and First-Principles Calculations. *Phys. Rev. Lett.* **2015**, *115*, 176801. [CrossRef] [PubMed]
74. Deilmann, T.; Drüppel, M.; Rohlfing, M. Three-particle correlation from a Many-Body Perspective: Trions in a Carbon Nanotube. *Phys. Rev. Lett.* **2016**, *116*, 196804. [CrossRef] [PubMed]

75. Rohlfing, M.; Louie, S.G. Electron-hole excitations and optical spectra from first principles. *Phys. Rev. B* **2000**, *62*, 4927–4944. [CrossRef]
76. Yu, H.; Liu, G.B.; Gong, P.; Xu, X.; Yao, W. Dirac cones and Dirac saddle points of bright excitons in monolayer transition metal dichalcogenides. *Nat. Commun.* **2014**, *5*, 3876. [CrossRef]
77. Mayers, M.Z.; Berkelbach, T.C.; Hybertsen, M.S.; Reichman, D.R. Binding energies and spatial structures of small carrier complexes in monolayer transition-metal dichalcogenides via diffusion Monte Carlo. *Phys. Rev. B* **2015**, *92*, 161404. [CrossRef]